Nuclear fragmentation cross section measurements for a 400 MeV/nucleon ^{16}O beam on polyethylene and hydrogen targets with the FOOT experiment

M. Dondi,[1,2,*] R. Ridolfi,[1,2] M. Toppi,[3,4] A. Mengarelli,[1] A. Alexandrov,[5] B. Alpat,[6] G. Ambrosi,[6] S. Argirò,[7,8] M. Barbanera,[6] N. Bartosik,[8,9] G. Battistoni,[10] V. Boccia,[11,5] G. Butella,[12] M. Caprai,[6] F. Cavanna,[8] P. Cerello,[8] E. Ciarrocchi,[13,14] N. D'Ambrosio,[15] G. De Lellis,[11,5] A. Di Crescenzo,[11,5] M. Donetti,[12] Y. Dong,[10] M. Durante,[11,16,17] R. Faccini,[18,4] V. Ferrero,[7,8] C. Finck,[19] E. Fiorina,[8] M. Francesconi,[5] M. Franchini,[1,2] G. Franciosini,[3,4] G. Galati,[20,21] L. Galli,[14] M. Ionica,[6] A. Iuliano,[5] K. Kanxheri,[6] B. Kharpuse,[8] A. C. Kraan,[14] A. Lauria,[11,5] E. Lopez Torres,[22,8] M. Magi,[3,4] A. Manna,[1,2] M. Marafini,[23,4] S. Masci,[15] M. Massa,[14] C. Massimi,[1,2] I. Mattei,[10] S. Mazzolani,[24,6] A. Mereghetti,[12] R. Mirabelli,[3,4] A. Moggi,[14] M. C. Montesi,[25,5] M. C. Morone,[26,27] M. Morrocchi,[13,14] S. Muraro,[10] N. Pastrone,[8] V. Patera,[3,4] F. Pennazio,[8] C. Pisanti,[1,2] P. Placidi,[6] M. Pullia,[12] F. Quattrini,[18,4] S. Rabaglia,[1] L. Ramello,[8,9] C. Reidel,[16] L. Sabatini,[28] L. Salvi,[6] C. Sanelli,[28] A. Sarti,[3,4] O. Sato,[29] S. Savazzi,[12] A. Schiavi,[3,4] C. Schuy,[16] E. Scifoni,[30] L. Servoli,[6] G. Silvestre,[6] M. Sitta,[9,8] B. Spadavecchia,[7,8] R. Spighi,[1,2] E. Spiriti,[28] L. Testa,[18,4,23] V. Tioukov,[5] S. Tomassini,[28] F. Tommasino,[31,30] G. Traini,[4] A. Trigilio,[28] G. Ubaldi,[1,2] S. Valentinetti,[1,2] M. Vanstalle,[19] U. Weber,[16] R. Zarrella,[1,2] A. Zoccoli,[1,2] and M. Villa[1,2]

(FOOT Collaboration)

[1]*INFN Section of Bologna, Bologna, Italy*

[2]*Department of Physics and Astronomy, University of Bologna, Bologna, Italy*

[3]*Department of Basic and Applied Sciences for Engineering, Sapienza University of Rome, Rome, Italy*

[4]*INFN Section of Rome, Rome, Italy*

[5]*INFN Section of Napoli, Napoli, Italy*

[6]*INFN Section of Perugia, Perugia, Italy*

[7]*Department of Physics, University of Torino, Torino, Italy*

[8]*INFN Section of Turin, Turin, Italy*

[9]*Department of Science and Technological Innovation, University of Piemonte Orientale, Alessandria, Italy*

[10]*INFN Section of Milan, Milan, Italy*

[11]*Department of Physics "E. Pancini", University of Napoli, Napoli, Italy*

[12]*CNAO, National Center for Oncological Hadrontherapy, Pavia, Italy*

[13]*Department of Physics, University of Pisa, Pisa, Italy*

[14]*INFN Section of Pisa, Pisa, Italy*

[15]*INFN Section of Gran Sasso National Laboratories, Assergi (L'Aquila), Italy*

[16]*Biophysics Department, GSI Helmholtzzentrum für Schwerionenforschung, Darmstadt, Germany*

[17]*Institute of Condensed Matter Physics, Technische Universität Darmstadt, Darmstadt, Germany*

[18]*Department of Physics, Sapienza University of Rome, Rome, Italy*

[19]*Université de Strasbourg, CNRS, IPHC UMR 7871, F-67000 Strasbourg, France*

[20]*Department of Physics, University of Bari, Bari, Italy*

[21]*INFN Section of Bari, Bari, Italy*

[22]*CEADEN, Centro de Aplicaciones Tecnologicas y Desarrollo Nuclear, Havana, Cuba*

[23]*Museo Storico della Fisica e Centro Studi e Ricerche Enrico Fermi, Rome, Italy*

[24]*Department of Physics, University of Camerino, Camerino, Italy*

[25]*Department of Chemistry, University of Napoli, Napoli, Italy*

[26]*Physics Department, University of Roma Tor Vergata, Rome, Italy*

[27]*INFN Section of Roma Tor Vergata, Rome, Italy*

[28]*INFN Laboratori Nazionali di Frascati, Frascati, Italy*

[29]*Department of Physics, Nagoya University, Nagoya, Japan*

[30]*Trento Institute for Fundamental Physics and Applications, Istituto Nazionale di Fisica Nucleare (TIFPA-INFN), Trento, Italy*

[31]*Physics Department, University of Trento, Trento, Italy*

(Received 17 February 2026; revised 5 May 2026; accepted 2 June 2026; published 25 June 2026)

*Contact author: mdondi@bo.infn.it

The measurement of fragmentation cross sections for nuclei up to ^{56}Fe on light elements found in the human body (e.g., H, C, and O) is of fundamental importance for particle therapy (PT) and radioprotection in space (RPS), as well as for advancing cosmic-ray physics. These measurements can significantly improve the accuracy of dose calculations for patients during PT treatments and for astronauts exposed to cosmic radiation during deep-space missions. Among the many ions of interest, ^{16}O is used in PT and is the most abundant species within the HZE component of cosmic rays. This paper presents the results of angular nuclear fragmentation cross sections for the production of He, Li, Be, B, C, and N nuclei in the interaction of a 400 MeV/nucleon ^{16}O beam with a hydrogen and polyethylene target. The fragmentation on the hydrogen was measured by combining the results on polyethylene with recent measurements on a graphite target. While the fragmentation on hydrogen is fundamental for improving nuclear interaction models, allowing more accurate predictions of dose distributions in PT and RPS, polyethylene has proven to be a promising shielding material in radiation protection models. The data analyzed were collected in 2021 at the GSI Helmholtz Center for Heavy Ion Research facility in Darmstadt (Germany) by the FOOT Collaboration. All results were compared with different Monte Carlo models for light ion fragmentation physics in the energy range of interest implemented in FLUKA and Geant4.

DOI: 10.1103/17nq-3ddt

I. INTRODUCTION

Nuclear fragmentation cross-section measurements have a significant impact across various scientific fields, particularly in particle therapy (PT) and space radioprotection (RPS) for the safety of human space missions [1,2], as well as in cosmic-ray physics [3]. In PT, nuclear interactions of primary ion beams with the human body leads to the production of secondary fragments. The availability of fragmentation cross section measurements is fundamental for having accurate predictions of dose distribution within human tissue, thereby minimizing damage to healthy cells and determining the biological effectiveness of therapies [4–6]. Similarly, accurate fragmentation data are essential for assessing radiation risks to astronauts from Galactic Cosmic Radiation (GCR) and Solar Particle Events (SPEs), facilitating the development of effective shielding strategies against these complex radiation environments [7–9].

Although these two fields of study are quite different, they exhibit some overlap in the types of beams, targets, and energy ranges of interest. In PT, attention is focused on the fragmentation of light ions with $Z \leqslant 10$ interacting with elements that constitute the human body, mainly H, C, and O, in the energy range 100–600 MeV/nucleon [1]. Studies of fragmentation in RPS extend the investigation from hydrogen (^{1}H) to iron (^{56}Fe) over a broader energy interval, 100–1000 MeV/nucleon [2]. For RPS, the targets of interest are those employed in the optimization of astronaut shielding, which mainly consist of hydrogen-rich materials [10]. However, the limited availability and insufficient precision of fragmentation cross section measurements [11–13] prevent achieving the level of accuracy required for the calculation of the biological dose delivered by secondary fragments in PT and RPS applications [14,15].

While some key measurements have been performed already [16–25], they still cover only a limited set of beam-target-energy configurations. In order to measure the missing fragmentation cross sections for these applications, dedicated experimental campaigns are needed to fill these gaps. A systematic measurement of the missing fragmentation cross sections would provide the necessary benchmarks to validate and improve the nuclear models currently implemented in Monte Carlo (MC) and deterministic transport codes, which are extensively used for dose evaluations in these contexts [26,27].

Fragmentation cross sections on a hydrogen target are essential to compute the dose deposited by fragments in both patients and astronauts with the required accuracy, as hydrogen, alongside carbon and oxygen, is one of the most abundant elements in the human body. While further data on hydrogen fragmentation for various ion beams are still needed, the fragmentation of ^{16}O is of particular interest. This ion is increasingly utilized in PT facilities alongside p,^{4}He, and ^{12}C [1]. Simultaneously, ^{16}O is the most abundant species among the HZE (high atomic number Z and energy E) components of cosmic rays after carbon [2,3], and it contributes significantly to the total dose, exceeded only by ^{56}Fe and ^{28}Si [2]. Since measuring ^{16}O fragmentation directly on a liquid hydrogen target is experimentally challenging (see Sec. III B), the cross sections can be derived via stoichiometric subtraction from measurements on C_2H_4 and C targets.

Notably, fragmentation cross sections of ^{16}O on C_2H_4 are also of direct interest for RPS applications. In this context, light materials seem to be particularly effective as shields against space radiation [2,7], and liquid hydrogen has the maximum performance as shield material. However, hydrogen is not a practical shield material, being a low temperature liquid, so polyethylene (C_2H_4) can be a good compromise [9,10]. The better shielding performance of light materials arises from their ability to maximize energy loss per unit mass, minimizing the production of secondary particles, which constitute a significant portion of the dose equivalent behind thick shields [9]. While aluminum shielding can lead to an increase in dose equivalent beyond approximately 20 g/cm^2 due to secondary particle buildup, polyethylene has been shown to monotonically reduce the dose equivalent with increasing thickness [10]. As shown in [10], significant discrepancies remain in the calculated dose beyond the shielding when different nuclear interaction models are employed. Accurate fragmentation cross sections for these specific beam-target combinations are essential to constrain and reduce such uncertainties.

The FOOT (FragmentatiOn Of Target) experiment was designed to address these data gaps, by measuring nuclear

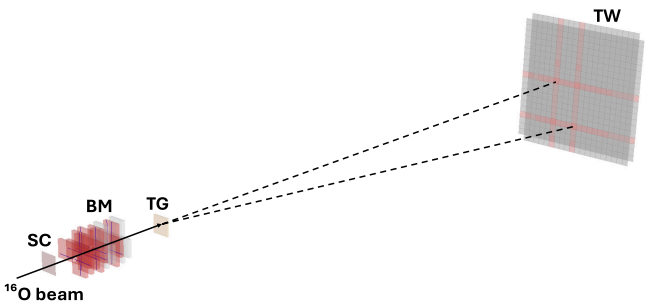

FIG. 1. Schematic representation of the GSI experimental setup.

fragmentation cross sections from interactions between various ion beams and targets relevant to both PT and RPS [28]. A detailed description of the FOOT experiment, along with some preliminary results, can be found in [23,24,28,29]. The data analyzed in this work were acquired during the same data taking campaign at the GSI Helmholtz Center for Heavy Ion Research in Darmstadt analyzed in [24], where the measurements of the fragmentation of a 400 MeV/nucleon ^{16}O beam interacting with a graphite target are described. At that stage, only a portion of the final FOOT detector, namely, the same setup used in [24], was available. The apparatus was composed of a beam monitor [30] before the target and a Time Of Flight (TOF) system [31,32]. These components enabled the identification of the fragment charge Z and the reconstruction of the emission angle.

This work presents the measurements of elemental integral and angular differential cross sections for the production of He, Li, Be, B, C, and N fragments, resulting from the interaction of a 400 MeV/nucleon ^{16}O beam with a 10 mm polyethylene (C_2H_4) target. By combining these results with the same measurements on a C target, described in [24], the fragmentation cross sections for a hydrogen target were finally derived (see Sec. III B).

These measurements provide new data for the fragmentation of ^{16}O on hydrogen and polyethylene, for which angular differential cross sections were previously unavailable in the literature to our knowledge. The hydrogen data are fundamental for improving nuclear interaction models, allowing more accurate predictions of dose distributions in PT and RPS.

II. MATERIALS AND METHODS

A. Experimental setup

The FOOT detector configuration adopted for this campaign was identical to that used in [24], where a detailed description of the experimental setup is provided.

The FOOT detector was installed in Cave-A (HTA) of the GSI facility. In Fig. 1 a schematic view of the experimental setup is shown. Upstream the target (TG), two detectors, the Start Counter (SC) [31] and the Beam Monitor (BM) [30], measured the incoming oxygen ions. Both detectors were designed with a minimal material budget to reduce pretarget fragmentation. All the setup operated in air. The SC, a 250 μm thick plastic scintillator, provided the TOF start with a resolution of about 50 ps, while the BM, a 12-layer wire drift chamber with X-Y readout, tracked the beam with spatial resolution better than 60 μm.

Downstream of the target, the TOF wall (TW) detector [32], composed of two orthogonal layers of plastic scintillator bars, measured the energy deposition ΔE with $\sigma(\Delta E)/\Delta E \sim 5\%$, the TOF stop with ∼20 ps resolution for ^{16}O ions [33] and the hit position of the fragments with a granularity of 2×2 cm^2 given by the bar crossing dimension. The TW was positioned 193 cm downstream from the target to ensure large acceptance and accuracy in the polar angle measurement for He and heavier fragments. The geometrical acceptance and detector granularity minimized pileup to below 1%, as shown by Monte Carlo simulations reported in [23,28]. The polar angle acceptance for this analysis is $\theta \leqslant 5.7^\circ$.

The charge Z identification (ZID) of each fragment was performed using the measurement of the energy ΔE deposited in the TW and the Time Of Flight (TOF) of the fragments through a parametrization of ΔE with a Bethe-Bloch as a function of the TOF [23]. Each fragment was associated with a pair of orthogonal bars (X and Y), forming a TW point. Only bar pairs with consistent reconstructed charge were clustered [23,24].

B. Data sample

Two data samples were collected: one with a ^{16}O beam of 400 MeV/nucleon impinging on a 10 mm polyethylene (C_2H_4) target and another acquired without target. The second sample was used to evaluate the background due to the fragmentation of the beam occurring outside the target, in the air crossed by the beam along its path and in the FOOT setup itself (see Sec. III). In particular, the present analysis makes use of the very same no-target dataset used in [24].

The data sample with the polyethylene target was collected using two different trigger strategies: the Minimum Bias (MB) trigger was issued whenever a primary ion of ^{16}O goes through the SC, while the fragmentation trigger (FRAG) rejected most of the primary oxygen ions reaching the TW, and was issued in presence of TW hits due to fragments of interest for cross section measurement. More details about the trigger strategies adopted can be found in [24,34]. The total numbers of events collected with the MB trigger were 4.38×10^6 and 1.07×10^6 for the FRAG trigger. During MB runs the information on whether the FRAG trigger conditions would have been satisfied was also stored, allowing the determination of the fraction of MB events that would have been labeled as FRAG. By exploiting this, the ratio between the number of events fulfilling the FRAG conditions and the total number of MB events was computed. This ratio, referred to as the FRAG *trigger acceptance factor* $\varepsilon_{\text{trig}}^{\text{FRAG}}$, was found to be $(17.73 \pm 0.03)\%$. Approximately 5.71×10^4 events were collected with the MB trigger in the configuration without the target, for background evaluation purposes. In Fig. 2, the effect of the FRAG trigger compared to the MB is evident from the energy released in the TW.

C. Monte Carlo simulation

Corresponding to the two data samples, two detailed Monte Carlo (MC) simulations of the full apparatus were carried

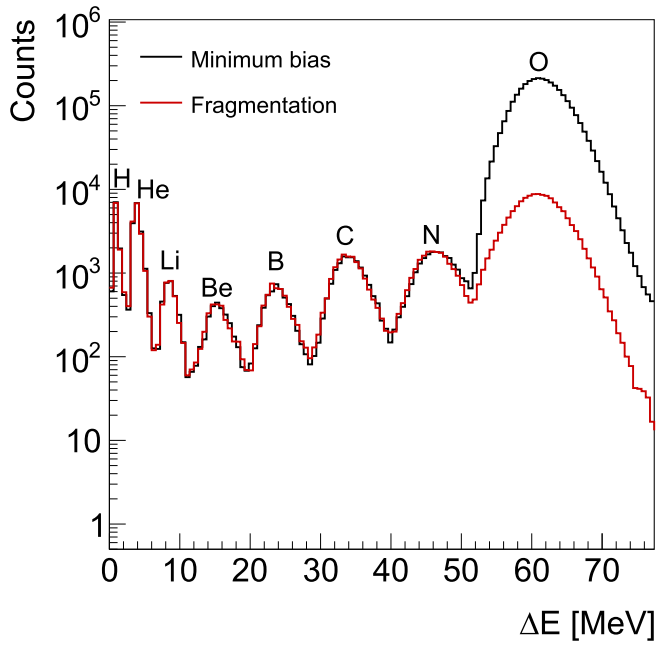

FIG. 2. Energy loss distribution in the TW central bars. The impact of the fragmentation trigger is evident from the suppression of the last peak corresponding to the energy release of the oxygen ion beam.

out using the FLUKA Monte Carlo code [35]: one with a polyethylene target and one without a target, consisting of 10^7 and 1.5×10^7 events, respectively. The simulations accurately reproduced the detector geometry, passive materials, and alignment adjustments [36]. The spatial resolution of the BM, the energy loss, and TOF resolutions in SC and TW were extracted from data as described in [23,30–32] and used for a Gaussian smearing of the quantities computed by FLUKA. In the following, quantities extracted directly from FLUKA at production level, before any detector simulation, digitization, or reconstruction is applied, are referred to as true MC quantities. For example, Z_{true} and θ_{true} denote the charge and emission angle of a fragment as produced in the target by FLUKA. In the same way the true MC cross section in the text refers to the FLUKA cross section at production level. The Monte Carlo simulations were used to evaluate reconstruction efficiencies and apply MC corrections for all fragments, to unfold the angular distributions, and to validate the analysis strategy adopted to measure the fragmentation cross sections, as described in more detail in Sec. III A.

III. ANALYSIS STRATEGY

A. Polyethylene target cross section

The objective of the analysis was to extract angular cross sections for a 400 MeV/nucleon oxygen beam against a polyethylene target for the forward production of He, Li, Be, B, C, and N nuclei within the 5.7° angular acceptance of the setup. Integrating the angular differential cross section over the covered angular range, the elemental cross section for the production of each charge was obtained. The analysis strategy employed for this measurement is summarized in the following and it is the same described in more detail in [24].

The formula for the angular cross section can be obtained as follows:

$$\frac{\mathrm{d}\sigma}{\mathrm{d}\Omega}(Z,\theta) = \frac{Y(Z,\theta)}{N_{\text{prim}} N_{\text{TG}} \varepsilon(Z,\theta) \Delta\Omega}, \tag{1}$$

where $Y(Z,\theta)$ is the number of fragments of a given charge Z at a given angle θ, N_{prim} is the total number of primaries, N_{TG} is the number of interaction centers in the target, ε the efficiency correction, and $\Delta\Omega$ is the solid angle bin width. The number of interaction centers in the target is given by

$$N_{\text{TG}} = \frac{\rho d N_A}{A}, \tag{2}$$

where $\rho = 0.94$ g/cm^3 is the polyethylene target density, $d = 10$ mm is the target thickness, N_A is the Avogadro number, and $A = 28.0534$ g/mol is the molar mass of the ethylene monomer constituting the polyethylene. The angle θ is the angle between the track of the primary measured by the BM and the track of the fragment. This last track was reconstructed starting from the impact point of the primary on the target, and the impact point of the fragment on the TW. This reconstruction procedure was applied identically to both the target and no-target runs. The contribution of the out-of-target fragmentation, mainly in air and in the FOOT detectors, was taken into account using the run taken with the ^{16}O beam without a target. The yield of the fragments with charge Z at a given angle θ is then given by

$$\frac{Y(Z,\theta)}{N_{\text{prim}}} = \frac{Y_{\text{TG}}(Z,\theta)}{N_{\text{prim,TG}}} - \frac{Y_{\text{noTG}}(Z,\theta)}{N_{\text{prim,noTG}}}, \tag{3}$$

where $Y_{\text{TG}}(Z,\theta)/N_{\text{prim,TG}}$ is the number of fragments over the number of primaries for the run with the polyethylene target and $Y_{\text{noTG}}(Z,\theta)/N_{\text{prim,noTG}}$ is the same quantity in the case of the run without a target. $Y_{\text{TG}}(Z,\theta)/N_{\text{prim,TG}}$ was calculated as a weighted average between MB and FRAG data samples.

The number of primaries in MB runs is the number of events that overcome certain cuts for pileup removal on SC and BM in order to ensure a single primary particle for each event. As mentioned in Sec. II B, the number of primaries in FRAG runs was instead recovered by dividing the number of FRAG trigger events by the *trigger acceptance factor*. After the selection cuts and the rescaling, the numbers of primaries were 3.65×10^6 for MB runs and 4.15×10^6 in the case of FRAG trigger. The selected events in the background run were 5.24×10^4, for this reason the background statistics dominates the uncertainty in the cross section measurements. The minimum angular bin width was chosen according to the TW granularity, and it is 0.6°. The total production cross section for each different charge was obtained by integrating the angular cross section in the angular acceptance of the experiment of 5.7°:

$$\sigma(Z) = \int_{\Omega} \frac{\partial\sigma}{\partial\Omega} = \frac{Y(Z)}{N_{\text{prim}} N_{\text{TG}} \varepsilon(Z)}. \tag{4}$$

The MC simulation (Sec. II B) was used to compute the efficiencies and the corrections needed in the measurement of the fragmentation cross sections [Eqs. (1) and (4)] and to verify the analysis strategy. A purity correction, discussed in Sec. III A 1, was introduced to correct the fragmentation yield $Y(Z,\theta)$ to take into account the misidentification of the Z charge due to the ZID algorithm of TW detector. The efficiency, described in Sec. III A 3, was used to recover the fragments lost in the reconstruction process.

The reconstructed MC cross sections, obtained using the analysis workflow described above, differential in angle for each charge Z, were compared to the true MC production values, defined by selecting fragments with known $(Z_{\text{true}}, \theta_{\text{true}})$ produced within the TW angular acceptance ($\theta_{\text{true}} \leqslant 5.7^{\circ}$). A residual discrepancy between reconstructed and true MC cross sections was observed and attributed to the migration between angular bins caused by the TW limited granularity. This discrepancy was corrected with an angular unfolding procedure in the analysis (see Sec. III A 2), which allowed us to dramatically improve the agreement between reconstructed and true MC cross section, especially in the case of carbon ($Z = 6$) and Nnitrogen ($Z = 7$) fragments, for which a narrow angular distribution is expected [28]. In the analysis, the raw yields, obtained from subtracting the data without target from the data with target, were corrected using purity, then the angular unfolding was applied and finally the efficiency. The full analysis workflow, considering background subtraction, purity correction, angular unfolding, and efficiency correction, was validated on MC, comparing the obtained cross section with the FLUKA production cross section and was applied identically to data. The final results for the charge-changing and elemental cross sections are reported in Sec. IV.

1. Purity correction

The charge identification (ZID) of the TW detector relied on energy loss (ΔE) and time-of-flight (TOF) measurements [23]. Due to finite resolution, a purity correction was introduced to account for Z misidentification. It is defined as

$$P(Z,\theta) = \frac{N(Z_{\text{reco}} = Z_{\text{true}}, \theta_{\text{reco}})}{N(Z_{\text{reco}}, \theta_{\text{reco}})}, \tag{5}$$

and applied as a multiplicative factor to the raw yield in Eq. (3). Similarly to the results of [24], the purity exceeded 90% for most fragment charges, except for lithium ($Z = 3$), where the value dropped to 70%. The drop was due to unavoidable contamination from two collinear He fragments depositing an energy comparable to Li in the TW, leading to Li misidentification (see the description of this process also in [17]).

2. Angular unfolding

When extracting angular differential cross sections, detector effects on the reconstructed polar angle, dominated by multiple Coulomb scattering and TW granularity, were corrected with a Bayesian iterative unfolding ([37–39]) implemented in RooUnfold [40]. The procedure, as described in [24], foresaw the construction of a two-dimensional response matrix C_{ij}, derived from simulation, that relates the reconstructed angle θ_{reco} measured with respect to the incident ^{16}O beam to the true production angle θ_{true} of fragments emerging from the target. The latter is defined as the emission angle of the fragment at the target exit, since intratarget scattering was found to be negligible. In this way both acceptance and resolution migrations were encoded. The spectrum of the measured fragments and C_{ij} define a likelihood that is iteratively updated, starting from the MC distribution as the prior; three iterations, chosen by minimizing the average correlation factor, achieve a balance between stability and statistical fluctuations.

3. Efficiency correction

The efficiency $\varepsilon(Z,\theta)$ was evaluated for each fragment charge Z and emission angle θ to account for fragments not reconstructed by the TW detector. It also included fragments produced in the target and within the TW acceptance ($\theta \leqslant 5.7^{\circ}$) but not reaching the detector due to multiple Coulomb scattering or interactions in air. The efficiency is defined as

$$\varepsilon(Z,\theta) = \frac{N_{\text{TW}}(Z,\theta)}{N_{\text{prod}}(Z,\theta)}, \tag{6}$$

where N_{TW} is the number of fragments with true charge Z and angle θ reconstructed by the TW, and N_{prod} is the number of fragments produced in the target within the TW acceptance. The dominant contribution to the efficiency loss arised from TW reconstruction. In fact, in order to have a clean Z identification, only pairs of X-Y bars sharing the same reconstructed Z were selected and clusterized in a TW point. X-Y bars with different Z charge were rejected and not clusterized as a TW point. The efficiency reduction was particularly significant for light fragments (He, Li) due to higher track density and overlapping hits [23,24] in the forward region (small angles), as can be seen in Fig. 3, where the efficiencies of the different fragments as a function of angle are shown.

B. Hydrogen target cross section

The cross section measurements for a carbon target presented in [24] were obtained under the same beam conditions, detector setup, and analysis procedures as those used in this work. For this reason, the results from [24] can be directly combined with the present data to determine the cross section for a hydrogen target.

The use of a dedicated hydrogen target was avoided because liquid hydrogen requires cryogenic conditions (around $T \simeq 20$ K) and involves significant technical and safety challenges, making its handling and long-term stability particularly complex. Furthermore, the use of liquid hydrogen or gaseous hydrogen at feasible pressures would result in a very low target density, making the measurement inefficient within reasonable beam times. Therefore, a stoichiometric subtraction between polyethylene (C_2H_4) and carbon data to isolate the hydrogen contribution was adopted. This subtraction method was already used to calculate differential cross section results and validated in [18]. The angular differential

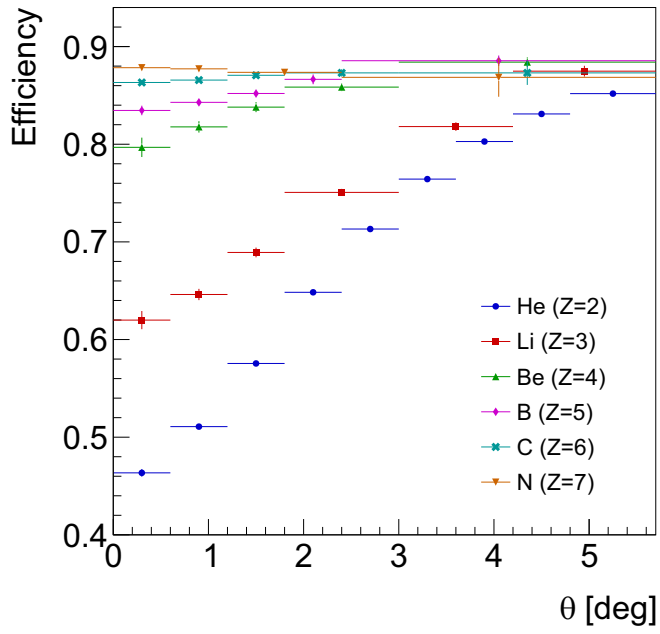

FIG. 3. Efficiencies of the different fragments as a function of angle.

cross section for a hydrogen target was extracted as

$$\frac{d\sigma}{d\Omega}[H] = \frac{1}{4}\left(\frac{d\sigma}{d\Omega}[C_2H_4] - 2\frac{d\sigma}{d\Omega}[C]\right) \quad (7)$$

where the coefficients reflect the 2:4 C:H stoichiometry of the ethylene monomer after normalizing to nuclei and correcting for target areal densities and detector efficiencies.

C. Systematic uncertainties

Several sources of systematic uncertainty were identified in the analysis, affecting both the detector response and the analysis procedure. Detector- level reconstruction systematics were evaluated by modifying the reconstruction or calibration strategy, or by varying the parameters used in reconstruction, and then propagating the resulting changes through the full cross-section analysis chain. For each analysis bin, the percentage change of the resulting cross section with respect to the nominal one was taken as the associated systematic uncertainty.

Two detector-level sources were investigated in detail: the event selection based on the BM, and the requirements applied to fragment reconstruction within the TW. The first one was studied varying the selection criteria for the BM reconstructed tracks and was found to be negligible. The second detector-level contribution was related to the charge reconstruction in the TW. In Monte Carlo simulation the resolution of energy loss (ΔE), time of flight (TOF), and position, all observables entering fragment identification, were varied within their experimental precision and the full analysis was repeated. Only a small effect was observed, below 0.5%. To probe the impact on the Z identification (ZID), the Bethe-Bloch parametrized curves, obtained from fits to ΔE versus TOF distributions at true MC level, were shifted within their statistical uncertainties; the induced variations were negligible (<0.5%) for all fragments, with the largest values being observed for helium. In addition, the TW calibration strategy was tested: each ΔE peak was fitted and calibrated to the MC value using a Birks fit [23,32,33]; shifting the fitted mean value within its statistical uncertainty produced effects in the range 0.1–2%. The systematic uncertainty associated with the unfolding procedure was assessed by repeating the unfolding of the MC angular distribution with an alternative algorithm. The nominal method is Bayesian iterative; as a cross-check the Iterative Dynamically Stabilized (IDS) method [41] was applied using the same number of iterations. Differences between the two unfolded spectra fell in the interval 0.1–3.6%, with the largest deviations occurring in certain angular bins for the heavier fragments.

TABLE I. Elemental nuclear fragmentation cross sections for a 400 MeV/nucleon ^{16}O beam on a polyethylene target, integrated over the solid angle covered by the FOOT setup ($\theta \leqslant 5.7^{\circ}$). Statistical and systematic uncertainties are reported separately.

Element	$\sigma \pm \Delta_{stat} \pm \Delta_{sys}$ (mb)	Δ_{stat}/σ	Δ_{sys}/σ
He	$2185 \pm 30 \pm 94$	1.4%	4.3%
Li	$183 \pm 8 \pm 7$	4.2%	3.9%
Be	$117 \pm 6 \pm 4$	5.6%	3.7%
B	$220 \pm 8 \pm 9$	3.7%	4.1%
C	$524 \pm 14 \pm 20$	2.6%	3.9%
N	$476 \pm 14 \pm 15$	3.0%	3.2%

The validity of the full reconstruction procedure, including the background subtraction to account for out-of-target fragmentation and the unfolding procedure, was also examined. As described in Sec. III A, the analysis method was validated by comparing the reconstructed MC cross sections, obtained after all the analysis steps, which were also applied to data, with the true MC cross sections. The observed difference included the intrinsic limitations of the full strategy and was therefore taken as a systematic contribution. Its impact spanned 0.3–3% for total cross sections and could reach values as high as 10% in angular differential cross sections. Given its value relative to the other evaluated sources, this contribution represented the dominant systematic, especially in the angular distributions. The numerical evaluation of all systematic contributions entering the cross section measurements is reported in Tables I, II, III, and IV.

The hydrogen cross section was obtained by subtracting the carbon contribution from that measured on the C_2H_4 target, as described in Eq. (7). The systematic uncertainty associated with this procedure was evaluated through two distinct contributions, treated as relative uncertainties and combined to provide the total systematic uncertainty on the hydrogen result.

The first, dominant, source of uncertainty was defined as the relative difference between the hydrogen cross section, derived from the subtraction of the MC reconstructed C_2H_4 and C cross sections, and that obtained from the subtraction of the corresponding true cross sections in the MC simulation. This term was closely related to the validity test discussed

TABLE II. Angular differential cross sections for a 400 MeV/nucleon ^{16}O beam on a polyethylene target. Statistical and systematic uncertainties are reported separately.

Z	θ (deg)	$d\sigma/d\Omega \pm \Delta_{stat} \pm \Delta_{sys}$ (b sr^{-1})	Δ^{rel}_{stat}	Δ^{rel}_{sys}
He	0–0.6	$431 \pm 33 \pm 19$	7.6%	4.4%
	0.6–1.2	$293 \pm 15 \pm 12$	5.0%	4.0%
	1.2–1.8	$206 \pm 8 \pm 7$	3.7%	3.5%
	1.8–2.4	$145 \pm 5 \pm 5$	3.4%	3.6%
	2.4–3.0	$104 \pm 3 \pm 4$	2.7%	3.7%
	3.0–3.6	$62.7 \pm 2.1 \pm 2.1$	3.3%	3.4%
	3.6–4.2	$43.2 \pm 1.4 \pm 1.5$	3.2%	3.5%
	4.2–4.8	$27.4 \pm 0.9 \pm 1.0$	3.4%	3.8%
	4.8–5.7	$15.2 \pm 0.6 \pm 2.2$	3.9%	14.5%
Li	0–0.6	$39.1 \pm 8.4 \pm 1.3$	21.5%	3.4%
	0.6–1.2	$30.8 \pm 3.9 \pm 1.0$	12.7%	3.2%
	1.2–1.8	$19.4 \pm 2.5 \pm 0.6$	13.1%	3.3%
	1.8–3.0	$11.8 \pm 0.7 \pm 0.5$	5.6%	4.5%
	3.0–4.2	$3.45 \pm 0.21 \pm 0.15$	6.1%	4.3%
	4.2–5.7	$0.81 \pm 0.05 \pm 0.06$	6.5%	7.2%
Be	0–0.6	$36.7 \pm 5.9 \pm 1.2$	16.0%	3.2%
	0.6–1.2	$25.0 \pm 3.1 \pm 0.8$	12.6%	3.0%
	1.2–1.8	$13.7 \pm 2.0 \pm 0.5$	14.7%	4.0%
	1.8–3.0	$6.34 \pm 0.63 \pm 0.27$	9.9%	4.2%
	3.0–5.7	$0.87 \pm 0.08 \pm 0.05$	9.3%	5.4%
B	0–0.6	$97.8 \pm 13.5 \pm 3.2$	13.8%	3.3%
	0.6–1.2	$70.0 \pm 4.0 \pm 2.7$	5.8%	3.9%
	1.2–1.8	$32.0 \pm 2.1 \pm 1.5$	6.6%	4.5%
	1.8–2.4	$13.9 \pm 1.1 \pm 0.7$	8.0%	5.1%
	2.4–5.7	$0.98 \pm 0.10 \pm 0.04$	10.0%	4.5%
C	0–0.6	$307 \pm 29 \pm 10$	9.5%	3.3%
	0.6–1.2	$198 \pm 6.8 \pm 10$	3.4%	5.1%
	1.2–1.8	$73.4 \pm 3.0 \pm 3.1$	4.0%	4.2%
	1.8–3.0	$14.4 \pm 0.7 \pm 0.7$	4.6%	5.2%
	3.0–5.7	$0.37 \pm 0.07 \pm 0.02$	19.4%	5.1%
N	0–0.6	$500 \pm 32 \pm 16$	6.5%	3.2%
	0.6–1.2	$199 \pm 7.0 \pm 10$	3.5%	5.0%
	1.2–2.4	$21.7 \pm 1.3 \pm 1.1$	6.2%	5.0%
	2.4–5.7	$0.32 \pm 0.04 \pm 0.02$	12.2%	5.4%

TABLE III. Elemental nuclear fragmentation cross sections for a 400 MeV/nucleon ^{16}O beam on a hydrogen target, integrated over the solid angle covered by the FOOT setup ($\theta \leqslant 5.7^\circ$). Statistical and systematic uncertainties are reported separately.

Element	$\sigma \pm \Delta_{stat} \pm \Delta_{sys}$ [mb]	Δ_{stat}/σ	Δ_{sys}/σ
He	$211 \pm 10 \pm 11$	4.6%	5.3%
Li	$17 \pm 3 \pm 1$	15%	3.9%
Be	$11 \pm 2 \pm 1$	20%	6.2%
B	$23 \pm 3 \pm 1$	12%	5.6%
C	$63 \pm 5 \pm 3$	7.2%	4.5%
N	$61 \pm 5 \pm 2$	7.9%	3.4%

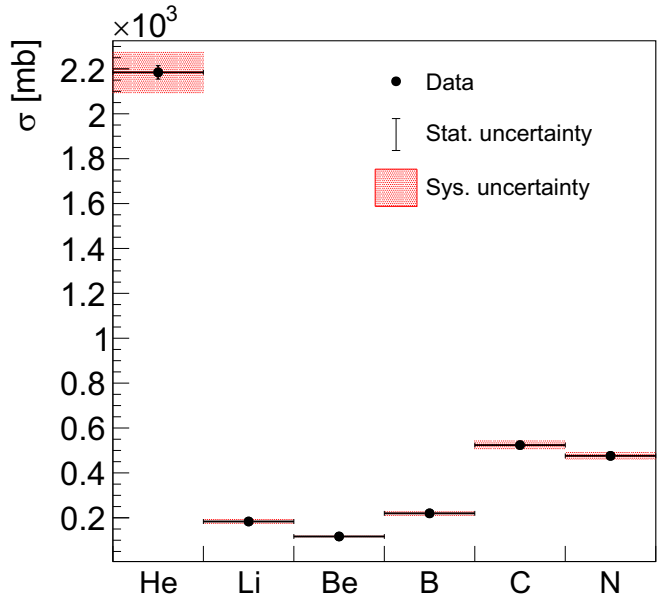

FIG. 4. Elemental nuclear fragmentation cross sections for the production of He, Li, Be, B, C, and N fragments in the interaction of a 400 MeV/nucleon ^{16}O beam with a polyethylene target, integrated over the solid angle covered by the FOOT setup ($\theta \leqslant 5.7^\circ$).

previously in Sec. III A, and it ranged from 0.2% to a maximum of 13%.

The second contribution accounted for the uncertainty related to the subtraction method itself. Within FLUKA, the hydrogen cross section directly predicted by the O-H interaction model was compared with the value obtained by subtracting the O-C MC cross section from the O-C_2H_4 MC cross section using Eq. (7). The relative difference observed in this comparison was smaller than the first contribution, and it was almost always below 1%, except in a few cases with a maximum value of 3%.

IV. RESULTS

A. Polyethylene target

Elemental and angular fragmentation cross sections for the production of He, Li, Be, B, C, and N fragments were measured for a 400 MeV/nucleon ^{16}O beam impinging on a polyethylene (C_2H_4) target. These cross sections refer to fragments emitted within the solid angle covered by the FOOT detector, corresponding to polar angles $\theta \leqslant 5.7^\circ$. The values were extracted following Eq. (1), using the fragments yields obtained from Eq. (3), after applying the purity correction and the unfolding procedure, as explained in Sec. III A. As in [24], although the beam was delivered at a nominal energy of 400 MeV/nucleon, the effective energy per nucleon at the center of the target was slightly lower due to upstream energy losses. Monte Carlo simulations estimated this effective value to be approximately 393 MeV/nucleon. The results for the elemental integral cross sections are shown in Fig. 4 and the corresponding numerical values are reported in Table I, with statistical and systematic uncertainties. In

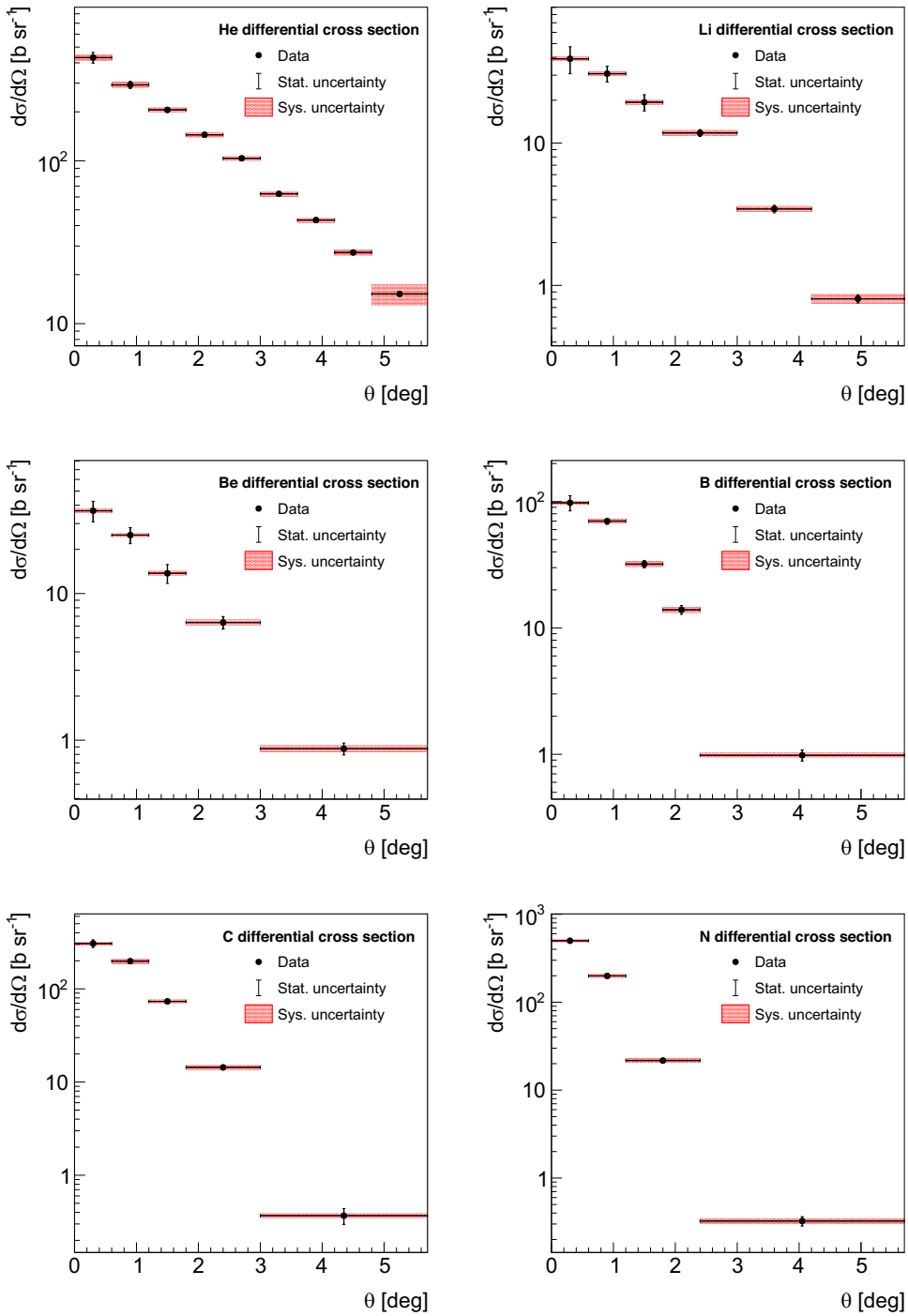

FIG. 5. Angular differential nuclear fragmentation cross sections for the production of He, Li, Be, B, C, and N fragments in the interaction of a 400 MeV/nucleon ^{16}O beam with a polyethylene target, binned in angle θ, with $\theta \leqslant 5.7^{\circ}$.

Fig. 5 and Table II the angular differential cross sections for the production of He, Li, Be, B, C, and N fragments in the interaction of a 400 MeV/nucleon ^{16}O beam with a polyethylene target are shown. The number and width of the angular bins were chosen according to the available statistics of the no-target sample used for the background subtraction, in order to ensure a sufficient number of fragments in each bin. The limited statistics of this background run dominated the statistical uncertainties, which ranged on average from 3% to 22%, while the systematic uncertainties were generally smaller in most bins and for all Z with the exception of He fragments.

B. Hydrogen target

The cross section for the production of He, Li, Be, B, C, and N fragments for a 400 MeV/nucleon ^{16}O beam interacting with a hydrogen target was obtained using Eq. (7)

TABLE IV. Angular differential cross sections for a ^{16}O beam of 400 MeV/nucleon on a hydrogen target. Statistical and systematic uncertainties are reported separately.

Z	θ (deg)	$d\sigma/d\Omega \pm \Delta_{stat} \pm \Delta_{sys}$ (b sr^{-1})	Δ^{rel}_{stat}	Δ^{rel}_{sys}
He	0–0.6	$57 \pm 10 \pm 4$	18%	6.5%
	0.6–1.2	$32.4 \pm 4.7 \pm 2.6$	15%	7.9%
	1.2–1.8	$20.1 \pm 2.5 \pm 1.1$	12%	5.4%
	1.8–2.4	$14.5 \pm 1.6 \pm 0.6$	11%	4.0%
	2.4–3.0	$9.68 \pm 0.91 \pm 0.48$	9.4%	4.9%
	3.0–3.6	$5.72 \pm 0.68 \pm 0.22$	12%	3.8%
	3.6–4.2	$3.79 \pm 0.45 \pm 0.20$	12%	5.3%
	4.2–4.8	$2.12 \pm 0.30 \pm 0.16$	14%	7.4%
	4.8–5.7	$0.93 \pm 0.20 \pm 0.13$	21%	14%
Li	0–0.6	$4.5 \pm 2.7 \pm 0.5$	61%	11%
	0.6–1.2	$2.9 \pm 1.3 \pm 0.1$	44%	3.4%
	1.2–1.8	$1.86 \pm 0.83 \pm 0.09$	45%	4.8%
	1.8–3.0	$1.03 \pm 0.22 \pm 0.08$	21%	8.2%
	3.0–4.2	$0.274 \pm 0.069 \pm 0.017$	25%	6.3%
	4.2–5.7	$0.057 \pm 0.017 \pm 0.006$	30%	10%
Be	0–0.6	$3.3 \pm 2.0 \pm 0.2$	59%	5.0%
	0.6–1.2	$2.9 \pm 1.0 \pm 0.1$	36%	4.6%
	1.2–1.8	$1.34 \pm 0.68 \pm 0.11$	50%	8.0%
	1.8–3.0	$0.56 \pm 0.21 \pm 0.03$	37%	6.2%
	3.0–5.7	$0.066 \pm 0.027 \pm 0.006$	41%	8.6%
B	0–0.6	$10.6 \pm 4.5 \pm 0.8$	42%	7.6%
	0.6–1.2	$7.5 \pm 1.3 \pm 0.4$	18%	5.8%
	1.2–1.8	$3.30 \pm 0.70 \pm 0.14$	21%	4.3%
	1.8–2.4	$1.53 \pm 0.37 \pm 0.10$	24%	6.3%
	2.4–5.7	$0.105 \pm 0.033 \pm 0.006$	31%	6.2%
C	0–0.6	$35.1 \pm 9.6 \pm 1.1$	27%	3.1%
	0.6–1.2	$24.1 \pm 2.2 \pm 1.6$	9.3%	6.7%
	1.2–1.8	$8.82 \pm 0.99 \pm 0.38$	11%	4.3%
	1.8–3.0	$1.81 \pm 0.22 \pm 0.10$	12%	5.6%
	3.0–5.7	$0.045 \pm 0.024 \pm 0.003$	52%	5.5%
N	0–0.6	$46 \pm 11 \pm 2$	23%	3.3%
	0.6–1.2	$29.9 \pm 2.2 \pm 1.4$	7.5%	4.5%
	1.2–2.4	$3.10 \pm 0.45 \pm 0.13$	15%	4.2%
	2.4–5.7	$0.044 \pm 0.013 \pm 0.002$	30%	4.4%

for the angular differential cross section and an analogous formula for the integral cross section. The results obtained are shown in Figs. 6 and 7, with the numerical values listed in Tables III and IV. Also in this case, the dominant uncertainty was the statistical one, which was obtained considering the statistical uncertainty of the two measurements of graphite and polyethylene.

V. COMPARISON WITH LITERATURE

To our knowledge, there are no relevant measurements for He and Li at the energy considered in this work, while some data exist for $Z \geqslant 4$ for different beams on a graphite target [16,22], but no data seem to be available for a polyethylene target, for either integral or angular differential cross section. In the case of the hydrogen target, while no measurements of angular differential cross sections were found in the literature, a direct comparison of elemental cross sections for $Z > 4$ was possible with the results reported by Zeitlin and collaborators [17]. In that study, elemental cross sections were measured within an angular acceptance of 6.7°, using a 375 MeV/nucleon ^{16}O beam, slightly lower in energy than the one used in the present work. A meaningful comparison was possible only for B, C, and N fragments, despite the different angular coverage, given the predominantly forward emission of such fragments. In particular, the measured cross sections for B, C, and N were consistent with those reported in [17] within the experimental uncertainties. Furthermore, Webber and collaborators in [16] reported elemental cross section measurements at an energy of 441 MeV/nucleon, with an angular acceptance of 7.7°. In this case, elemental cross sections for the production of Be, B, C, and N were provided. These measurements were in good agreement with the present results, with the exception of nitrogen, for which Webber reported a higher value. A summary of these literature results is shown in Table V and in Fig. 8.

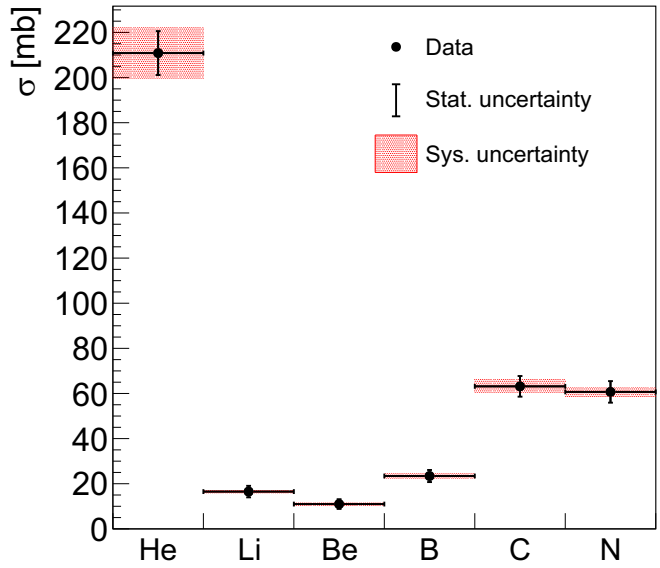

FIG. 6. Elemental nuclear fragmentation cross sections for the production of He, Li, Be, B, C, and N fragments in the interaction of a 400 MeV/nucleon ^{16}O beam with a hydrogen target, integrated over the solid angle covered by the FOOT setup ($\theta \leqslant 5.7°$).

VI. COMPARISON WITH NUCLEAR INTERACTION MODELS

The measured angular differential cross sections were compared against theoretical predictions obtained with four nuclear interaction models employed in Monte Carlo transport codes, as illustrated in Figs. 9 and 10. The models considered included FLUKA [35] and three hadronic models available in Geant4 [42–44]: the Binary Ion Cascade (BIC) [45], Quantum Molecular Dynamics (QMD) [46], and the Liège Intranuclear Cascade (INCL++) [47].

The Binary Ion Cascade (BIC) model was implemented through the G4IonPhysics class, a specialized physics library in Geant4 designed to handle ion-ion interactions. This

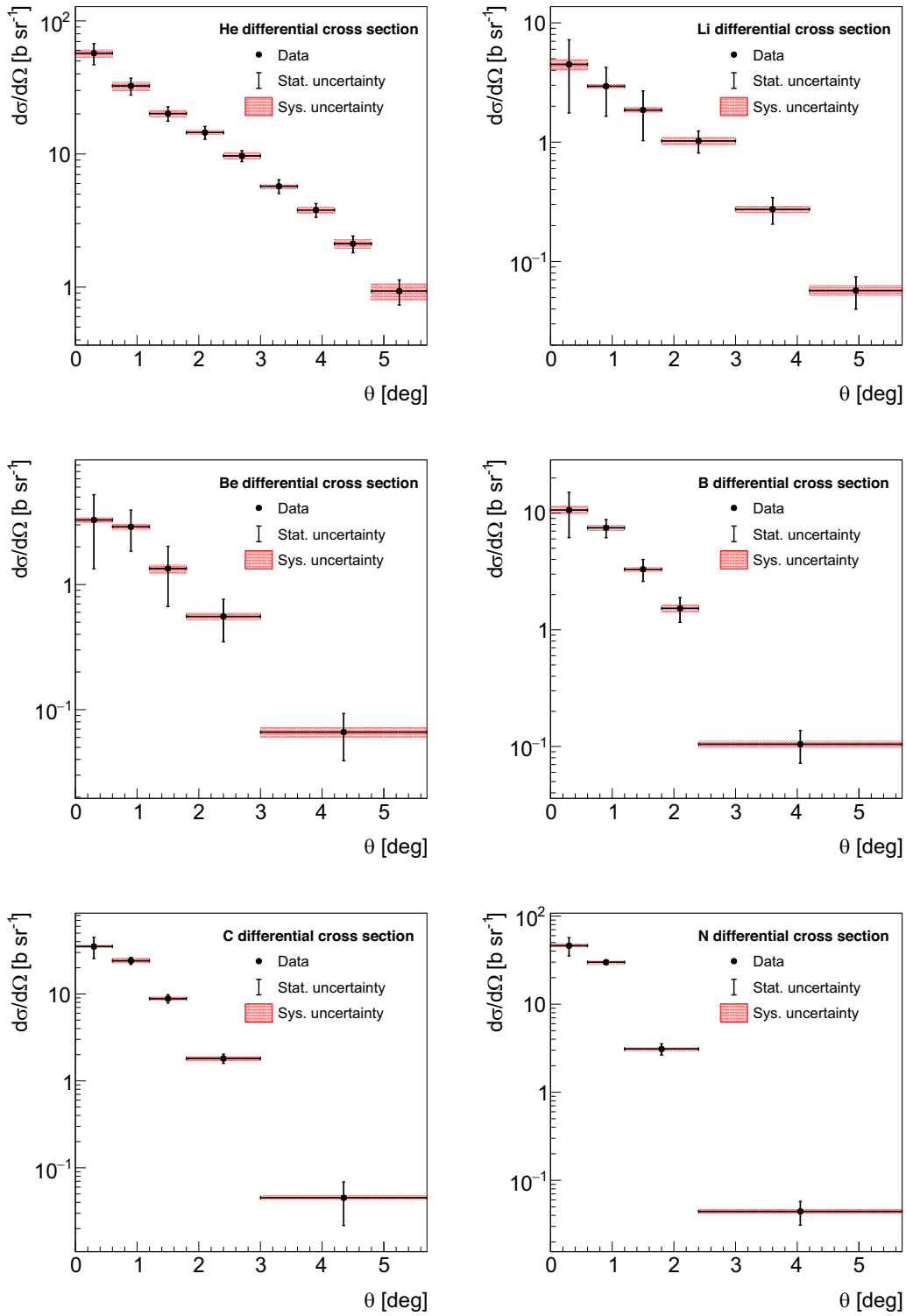

FIG. 7. Angular differential nuclear fragmentation cross sections for the production of He, Li, Be, B, C, and N fragments in the interaction of a 400 MeV/nucleon ^{16}O beam with a hydrogen target, binned in angle θ, with $\theta \leqslant 5.7^{\circ}$.

package incorporates a combination of models in order to cover a broad range of energies and interaction types for light ions (deuterons, tritons, ^{3}He, and α particles) as well as ions with $Z > 2$. This library employs Glauber-Gribov parametrizations for cross sections for all nucleus-nucleus collisions. At low energies, the Binary Ion Cascade model is coupled with the precompound/deexcitation model and subsequent deexcitation mechanisms, while for energies above 3 GeV/nucleon the simulation switches to the FTFP (Fritiof string model with precompound/deexcitation) approach.

The QMD model was implemented via the G4LightIonQMDPhysics library, which is adopted in

TABLE V. Literature values and results from this work of elemental nuclear fragmentation cross sections for $^{16}O + H$ interactions at similar beam energies. The beam energy refers to the energy at mid-target.

Ref.	Beam E_{Kin} (MeV/nucleon)	Angular accept.	Frag. Z	σ (mb)
This work	393	5.7°	Be	$11 \pm 2 \pm 1$
			B	$23 \pm 3 \pm 1$
			C	$63 \pm 5 \pm 3$
			N	$61 \pm 5 \pm 2$
Zeitlin [17]	375	6.7°	B	25 ± 2
			C	60 ± 4
			N	58 ± 4
Webber [16]	441	7.7°	Be	7.0 ± 0.7
			B	24.8 ± 1.2
			C	64.5 ± 3.2
			N	74.5 ± 3.7

applications such as hadron therapy and space radiation transport. In this approach, nucleons are represented as wave packets whose dynamical evolution follows the equations of quantum molecular dynamics, providing a more realistic description of nuclear interactions.

Both BIC and QMD models were complemented with G4HadronPhysicsQGSP_BIC, which provides a unified framework for hadronic interaction modeling. This library combines the Quark-Gluon String Precompound (QGSP) model with the Binary Intranuclear Cascade (BIC) model and is extensively used in different contexts, from high-energy physics experiments to applications in medical physics.

The third Geant4 model considered is INCL++, implemented via the G4IonINCLXXPhysics library, which describes nuclear reactions as a series of individual nucleon-nucleon collisions within the target nucleus. In this approach, nucleons are treated as a Fermi gas confined in a static potential well. During the interaction, projectile nucleons entering the target volume are identified as participants, while the other nucleons act as spectators. The fragmentation process is treated asymmetrically: the quasiprojectile is composed of projectile spectators and non-cascading participants, whereas the quasitarget results from the full cascade dynamics inside the calculation volume, providing a more accurate representation of the target remnant. INCL++ is particularly suited for simulating target fragmentation and is generally run in inverse kinematics. For reactions where both the projectile and target have mass numbers greater than $A = 18$, the simulation defaults to using the BIC model.

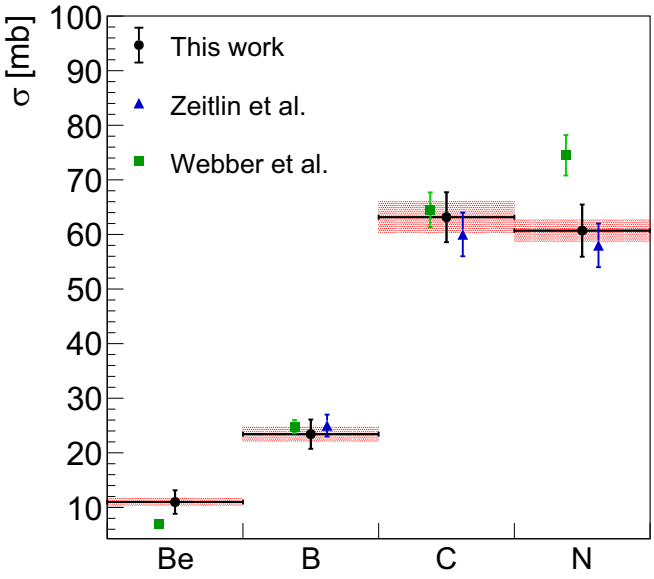

FIG. 8. Literature values and results from this work of elemental nuclear fragmentation cross sections for $^{16}O + H$ interactions.

In FLUKA simulations, for projectile energies above 150 MeV/nucleon, nucleus-nucleus interactions are modeled using a modified rQMD-2.4 (relativistic Quantum Molecular Dynamics) model, which can also operate as an intranuclear cascade [48–52]. While originally designed for high-energy collisions, this model can be applied to the energy range relevant for the FOOT experiment. The rQMD-2.4 is coupled with a preequilibrium stage managed by the PEANUT (PreEquilibrium Approach to Nuclear Thermalization) model [53,54], which is based on the GDH (Geometry Dependent Hybrid) exciton model [55]. The final stages of the interaction, fragmentation and evaporation, are treated for nuclei with $A < 17$ using a phase-space Fermi Breakup model [56,57].

Considering Figs. 9 and 10, it is evident that the BIC model systematically underestimates the cross sections for all fragments, producing distributions that are significantly flatter than both the experimental data and the predictions of the other models. FLUKA provides a good description for the lighter fragments, closely matching the experimental data, but underestimates the cross sections for B, C, and N at larger angles, resulting in distributions that are narrower than observed. INCL++ generally performs very well across most fragments, although it underpredicts the cross section for Be in the case of polyethylene and overpredicts it for He and Li for both polyethylene and hydrogen targets. QMD exhibits very good agreement with the data, showing behavior very similar to INCL++ while performing slightly better for Be and Li.

Overall, all models provided a reasonable description of the data, except for BIC, which clearly failed to reproduce the observed trends.

VII. CONCLUSIONS

In this work the measurement of elemental and angular nuclear fragmentation cross sections was presented for the production of He, Li, Be, B, C, and N fragments in the interaction of a 400 MeV/nucleon ^{16}O beam with a 10 mm polyethylene target. By combining these results with those obtained in a previous FOOT study [24], where the fragmentation cross sections of the same beam on a carbon target were measured, the cross sections for a hydrogen target were derived through a stoichiometric subtraction of the two measurements, as described in Sec. IV B.

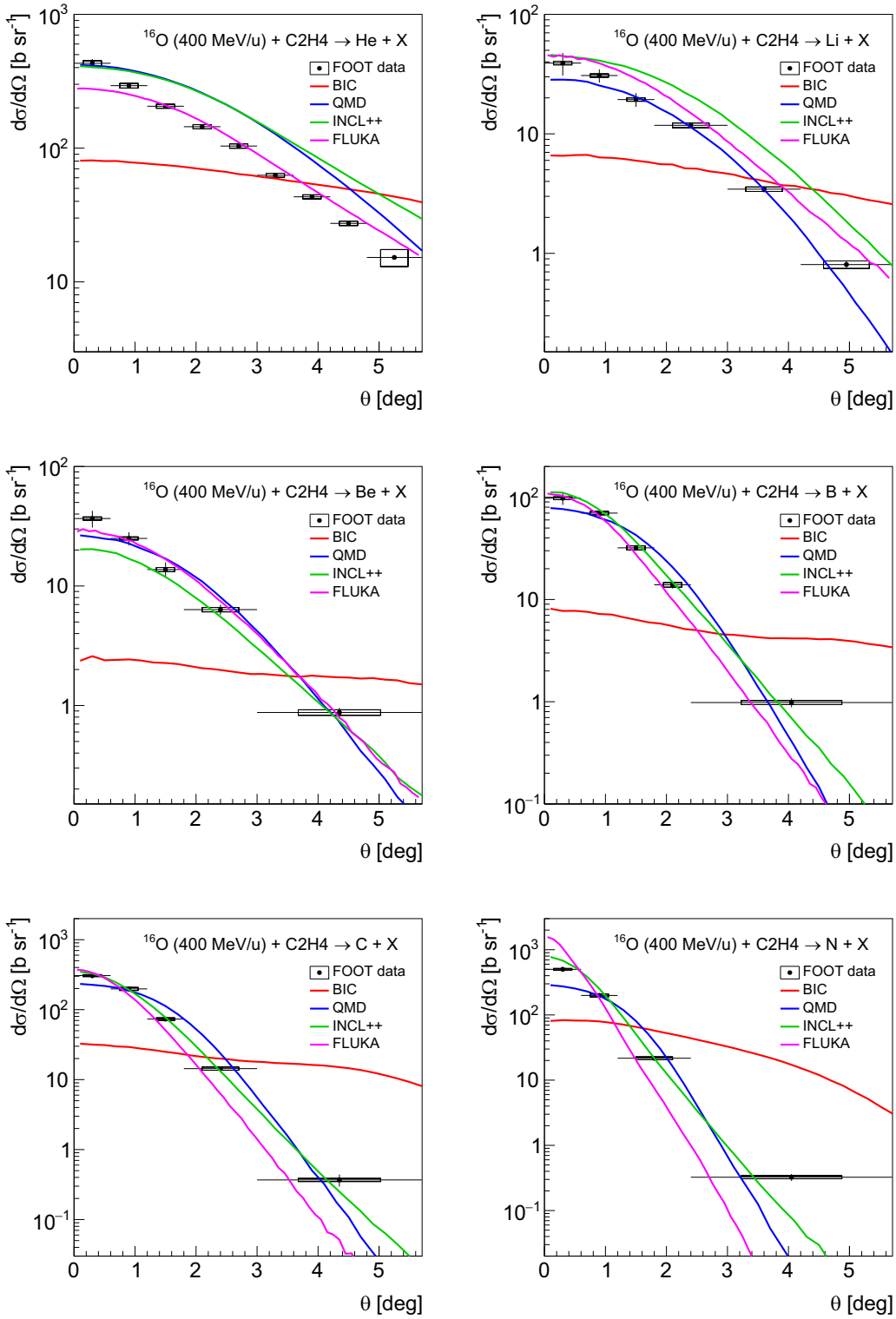

FIG. 9. Angular differential nuclear fragmentation cross sections for the production of He, Li, Be, B, C, and N fragments in the interaction of a 400 MeV/nucleon ^{16}O beam with a polyethylene target, together with FLUKA and Geant4 predictions with four different models.

The measurements were performed with a partial FOOT setup, allowing charge identification and the determination of the production angle of the fragments to obtain the angular cross sections. The overall precision was dominated by systematic uncertainties, mainly related to background subtraction, as for [23,24].

The results obtained for oxygen on polyethylene represent the first measurements of this target material, therefore no

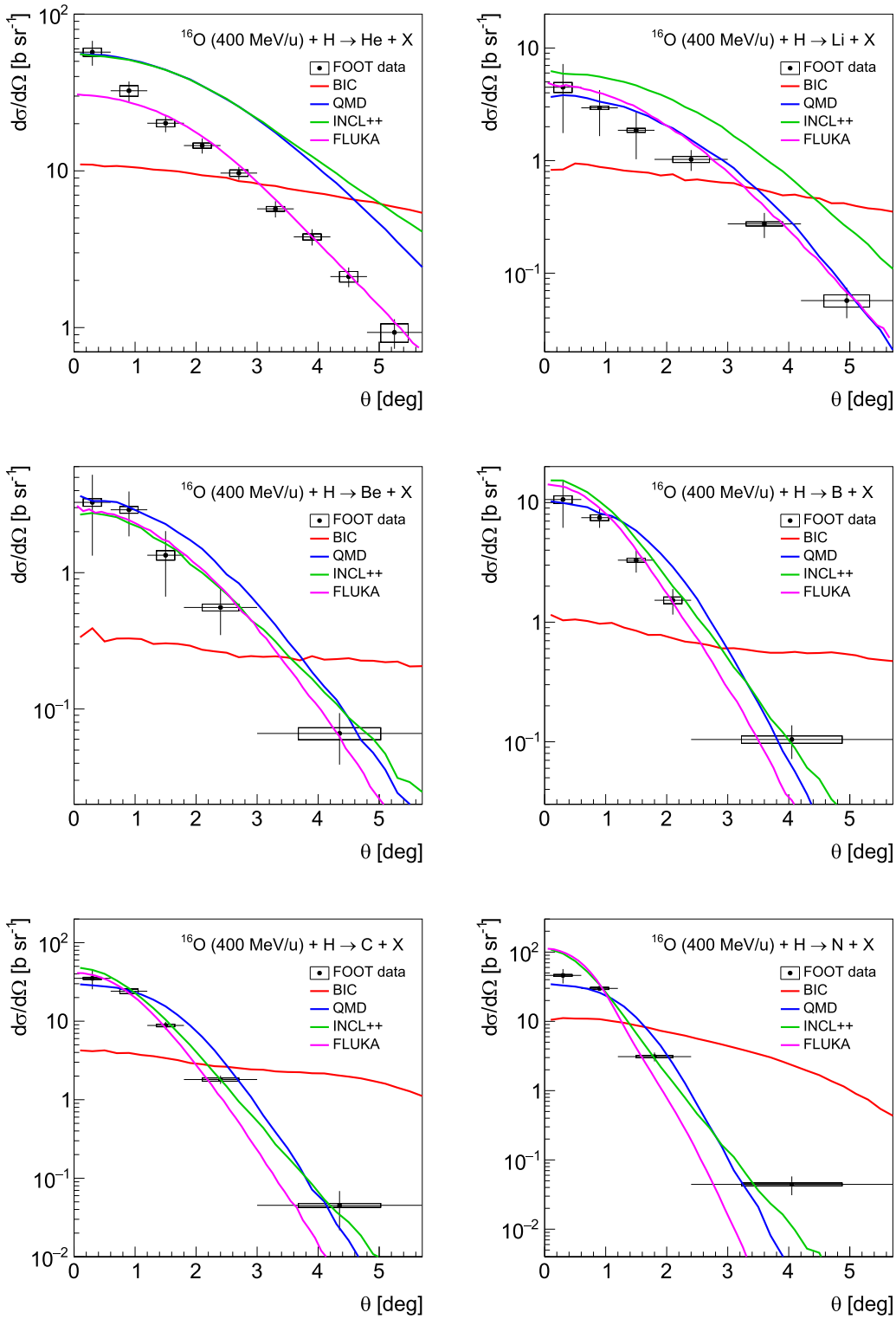

FIG. 10. Angular differential nuclear fragmentation cross sections for the production of He, Li, Be, B, C, and N fragments in the interaction of a 400 MeV/nucleon ^{16}O beam with a hydrogen target, together with FLUKA and Geant4 predictions with four different models.

comparison with other measurements available in the literature was possible for either the angular or the elemental cross sections. Concerning the hydrogen target, the results for the total production cross sections of B, C, and N fragments, which are the only ones directly comparable with existing data, were found compatible with the results in [17]. The angular differential cross sections for these fragments were measured here for the first time in the current energy range.

A comparison of the results of this work with theoretical predictions from different nuclear interaction models was also

presented. The BIC model failed to reproduce the data obtained, both for polyethylene and hydrogen, confirming the result obtained in [24]. The FLUKA model performed pretty well, with the exception of the last bins of higher Z fragments that were underestimated. QMD and INCL++ models from Geant4 showed a very good agreement with experimental data, although for light fragments the results were slightly overestimated.

The novelty of these measurements, together with the results of [24], in particular the angular cross sections, can provide stringent constraints on nuclear models in this energy range, thereby helping to achieve, in the future, the higher level of accuracy required for predictions in the fields of PT and RPS.

ACKNOWLEDGMENTS

The data taking proposal has been approved by the Program Advisory Committee for Biophysics and Radio-Biology (8th Bio-PAC meeting) as part of the "Call for Proposals for Beam Time in 2021/2022," in the frame of the FAIR Phase-0. We thank GSI for the successful operation of their facilities during the data taking. The FOOT Collaboration acknowledges the INFN for its support in building and running the detector.

DATA AVAILABILITY

There are no publicly available research data or software supporting this manuscript. Requests for further information or data should be sent to the authors.

[1] M. Durante and H. Paganetti, Nuclear physics in particle therapy: A review, Rep. Prog. Phys. **79**, 096702 (2016).
[2] M. Durante and F. A. Cucinotta, Physical basis of radiation protection in space travel, Rev. Mod. Phys. **83**, 1245 (2011).
[3] D. Maurin *et al.*, Precision cross-sections for advancing cosmic-ray physics and other applications: A comprehensive programme for the next decade, Phys. Rep. **1161**, 1 (2026).
[4] M. Krämer and M. Durante, Ion beam transport calculations and treatment plans in particle therapy, Eur. Phys. J. D **60**, 195 (2010).
[5] D. I. Thwaites, Accuracy required and achievable in radiotherapy dosimetry: Have modern technology and techniques changed our views? J. Phys. Conf. Ser. **444**, 012006 (2013).
[6] F. Tommasino and M. Durante, Proton radiobiology, Cancers (Basel) **7**, 353 (2015).
[7] J. Wilson *et al.*, Shielding strategies for human space exploration, NASA Report No. CP-3360, 1997, https://ntrs.nasa.gov/api/citations/19980137598/downloads/19980137598.pdf.
[8] J. H. Heinbockel and others, Comparison of the transport codes HZETRN, HETC and FLUKA for a solar particle event, Adv. Space Res. **47**, 1079 (2011).
[9] M. Durante, Space radiation protection: Destination Mars, Life Sci. Space Res. **1**, 2 (2014).
[10] T. C. Slaba *et al.*, Optimal shielding thickness for galactic cosmic ray environments, Life Sci. Space Res. **12**, 1 (2017).
[11] J. W. Norbury *et al.*, Nuclear data for space radiation, Radiat. Meas. **47**, 315 (2012).
[12] F. Luoni *et al.*, Total nuclear reaction cross-section database for radiation protection in space and heavy-ion therapy applications, New J. Phys. **23**, 101201 (2021).
[13] J. W. Norbury *et al.*, Are further cross section measurements necessary for space radiation protection or ion therapy applications? Helium projectiles, Front. Phys. **8**, 565954 (2020).
[14] F. Sommerer, K. Parodi, A. Ferrari, K. Poljanc, W. Enghardt, and H. Aiginger, Investigating the accuracy of the FLUKA code for transport of therapeutic ion beams in matter, Phys. Med. Biol. **51**, 4385 (2006).
[15] T. Sato, Y. Kase, R. Watanabe, K. Niita, and L. Sihver, Biological dose estimation for charged-particle therapy using an improved PHITS code coupled with a microdosimetric kinetic model, Radiat. Res. **171**, 107 (2009).
[16] W. Webber, J. C. Kish, and D. A. Schrier, Individual charge changing fragmentation cross sections of relativistic nuclei in hydrogen, helium, and carbon targets, Phys. Rev. C **41**, 533 (1990).
[17] C. Zeitlin, J. Miller, S. Guetersloh, L. Heilbronn, A. Fukumura, Y. Iwata, T. Murakami, S. Blattnig, R. Norman, and S. Mashnik, Fragmentation of ^{14}N, ^{16}O, ^{20}Ne, and ^{24}Mg nuclei at 290 to 1000 MeV/nucleon, Phys. Rev. C **83**, 034909 (2011).
[18] J. Dudouet *et al.*, Double-differential fragmentation cross-section measurements of 95 MeV/nucleon ^{12}C beams on thin targets for hadron therapy, Phys. Rev. C **88**, 024606 (2013).
[19] J. Dudouet, M. Labalme, D. Cussol, C. Finck, R. Rescigno, M. Rousseau, S. Salvador, and M. Vanstalle, Zero-degree measurements of ^{12}C fragmentation at 95 MeV/nucleon on thin targets, Phys. Rev. C **89**, 064615 (2014).
[20] R. Pleskac *et al.* (FIRST Collaboration), The FIRST experiment at GSI, Nucl. Instrum. Methods Phys. Res. Sect. A **678**, 130 (2012).
[21] M. Toppi *et al.* (FIRST Collaboration), Measurement of fragmentation cross sections of ^{12}C ions on a thin gold target with the FIRST apparatus, Phys. Rev. C **93**, 064601 (2016).
[22] I. Mattei *et al.* (FOOT Collaboration), Measurement of ^{12}C fragmentation cross sections on C, O, and H in the energy range of interest for particle therapy applications, IEEE Trans. Radiat. Plasma Med. Sci. **4**, 269 (2020).
[23] M. Toppi *et al.* (FOOT Collaboration), Elemental fragmentation cross sections for a ^{16}O beam of 400 MeV/u kinetic energy interacting with a graphite target using the FOOT ΔE-TOF detectors, Front. Phys. **10**, 979229 (2022).
[24] R. Ridolfi *et al.* (FOOT Collaboration), Angular differential and elemental fragmentation cross sections of a 400 MeV/nucleon ^{16}O beam on a graphite target with the FOOT experiment, Phys. Rev. C **112**, 014610 (2025).
[25] Y. Dong *et al.* (FOOT Collaboration), Cross section measurements of large angle fragments production in the interaction of carbon ion beams with thin targets, Eur. Phys. J. A **62**, 55 (2026).
[26] T. T. Böhlen, F. Cerutti, M. Dosanjh, A. Ferrari, I. Gudowska, A. Mairani, and J. M. Quesada, Benchmarking nuclear models of FLUKA and GEANT4 for carbon ion therapy, Phys. Med. Biol. **55**, 5833 (2010).
[27] J. Dudouet, D. Cussol, D. Durand, and M. Labalme, Benchmarking GEANT4 nuclear models for hadron therapy with 95 MeV/nucleon carbon ions, Phys. Rev. C **89**, 054616 (2014).

[28] G. Battistoni *et al.* (FOOT Collaboration), Measuring the impact of nuclear interaction in particle therapy and in radio protection in space: The FOOT experiment, Front. Phys. **8**, 568242 (2021).
[29] G. Galati *et al.* (FOOT Collaboration), Charge identification of fragments produced in ^{16}O beam interactions at 200 MeV/n and 400 MeV/n on C and C_2H_4 targets, Front. Phys. **11**, 1327202 (2024).
[30] Y. Dong *et al.* (FOOT Collaboration), The drift chamber detector of the FOOT experiment: Performance analysis and external calibration, Nucl. Instrum. Methods Phys. Res. Sect. A **986**, 164756 (2021).
[31] G. Traini *et al.* (FOOT Collaboration), Performance of the ToF detectors in the FOOT experiment, Nuovo Cimento Soc Ital. Fis. C **43** (2020).
[32] M. Morrocchi *et al.* (FOOT Collaboration), Development and characterization of a ΔE-TOF detector prototype for the FOOT experiment, Nucl. Instrum. Methods Phys. Res. Sect. A **916**, 116 (2019).
[33] A. Kraan *et al.* (FOOT Collaboration), Charge identification of nuclear fragments with the FOOT time-of-flight system, Nucl. Instrum. Methods Phys. Res. Sect. A **1001**, 165206 (2021).
[34] L. Galli *et al.*, The fragmentation trigger of the FOOT experiment, Nucl. Instrum. Methods Phys. Res. Sect. A **1046**, 167757 (2023).
[35] G. Battistoni *et al.*, The FLUKA code: An accurate simulation tool for particle therapy, Front. Oncol. **6**, 116 (2016).
[36] Y. Dong *et al.* (FOOT collaboration), The FLUKA Monte Carlo simulation of the magnetic spectrometer of the FOOT experiment, Comput. Phys. Commun. **307**, 109398 (2025).
[37] S. Stefan, Data unfolding methods in high energy physics, EPJ Web Conf. **137**, 11008 (2017).
[38] G. D'Agostini, A multidimensional unfolding method based on Bayes' theorem, Nucl. Instrum. Methods Phys. Res. Sect. A **362**, 487 (1995).
[39] G. D'Agostini, Improved iterative Bayesian unfolding, arXiv:1010.0632.
[40] T. Adye, Unfolding algorithms and tests using RooUnfold, arXiv:1105.1160.
[41] B. Malaescu, An iterative, dynamically stabilized (IDS) method of data unfolding, https://arxiv.org/abs/1106.3107.
[42] S. Agostinelli *et al.*, Geant4 - a simulation toolkit, Nucl. Instrum. Methods Phys. Res. Sect. A **506**, 250 (2003).
[43] J. Allison *et al.*, Geant4 developments and applications, IEEE Trans. Nucl. Sci. **53**, 270 (2006).
[44] J. Allison *et al.*, Recent developments in Geant4, Nucl. Instrum. Methods Phys. Res. Sect. A **835**, 186 (2016).
[45] G. Folger, V. N. Ivanchenko, and J. P. Wellisch, The binary cascade - nucleon nuclear reactions, Eur. Phys. J. A **21**, 407 (2004).
[46] D. Mancusi, K. Niita, T. Maruyama, and L. Sihver, Stability of nuclei in peripheral collisions in the JAERI quantum molecular dynamics model, Phys. Rev. C **79**, 014614 (2009).
[47] D. Mancusi, A. Boudard, J. Cugnon, J.-C. David, P. Kaitaniemi, and S. Leray, Extension of the Liège intranuclear-cascade model to reactions induced by light nuclei, Phys. Rev. C **90**, 054602 (2014).
[48] H. Sorge, H. Stöcker, and W. Greiner, Relativistic quantum molecular dynamics approach to nuclear collisions at ultrarelativistic energies, Nucl. Phys. A **498**, 567 (1989).
[49] H. Sorge, Flavor production in Pb (160A GeV) on Pb collisions: Effect of color ropes and hadronic rescattering, Phys. Rev. C **52**, 3291 (1995).
[50] V. Andersen *et al.*, The FLUKA code for space applications: Recent developments, Adv. Space Res. **34**, 1302 (2004), special issue, Space Life Sciences: Radiation Risk Assessment and Radiation Measurements in Low Earth Orbit.
[51] H. Aiginger *et al.*, The FLUKA code: New developments and application to 1 GeV/n iron beams, Adv. Space Res. **35**, 214 (2005).
[52] F. Ballarini *et al.*, The physics of the FLUKA code: Recent developments, Adv. Space Res. **40**, 1339 (2007).
[53] A. Ferrari and P. R. Sala, The physics of high energy reactions, in *Proceedings of Workshop on Nuclear Reaction Data and Nuclear Reactors Physics, Design and Safety* (CERN, Geneva, 1997).
[54] A. Ferrari and P. Sala, Nuclear reactions in Monte Carlo codes, Radiat. Prot. Dosim. **99**, 29 (2002).
[55] M. Blann, Hybrid model for pre-equilibrium decay in nuclear reactions, Phys. Rev. Lett. **27**, 337 (1971).
[56] E. Fermi, High energy nuclear events, Prog. Theor. Phys. **5**, 570 (1950).
[57] M. Epherre and E. Gradsztajn, Calcul de la spallation de ^{12}C et ^{16}O par des protons de 70 a 200 MeV, J. Phys. **28**, 745 (1967).